# Basement topography and sediment thickness beneath Antarctica's Ross Ice Shelf imaged with airborne magnetic data

Matthew Davis Tankersley[1], Huw Joseph Horgan[1], Christine Smith Siddoway[2], Fabio Caratori Tontini[3], and Kirsteen Jane Tinto[4]

[1]Victoria University of Wellington
[2]Colorado College
[3]University of Genova
[4]Lamont-Doherty Earth Observatory

November 30, 2022

Posted on 30 Nov 2022 — CC-BY 4.0 — https://doi.org/10.1002/essoar.10509277/v1 — This a preprint and has not been peer reviewed. Data may be preliminary.

## Abstract

New geophysical data from Antarctica's Ross Embayment illuminate the structure and subglacial geology of subsided continental crust beneath the Ross Ice Shelf. We use airborne magnetic data from the ROSETTA-Ice Project (2015-2019) to locate the basement-cover contact and map the extent of sedimentary basins. We delineate a broad, segmented high with thin (0-500 m) sedimentary cover which trends northward into the Ross Sea's Central High. Before subsiding below sea level, this feature likely facilitated early glaciation in the region and subsequently acted as a pinning point and ice flow divide. Flanking the high are wide basins, up to 3700 m deep, parallel with Ross Sea basins, which likely formed during Cretaceous-Neogene intracontinental extension. NW-SE basins beneath the Siple Coast grounding zone, by contrast, are narrow, deep, and elongate. They suggest tectonic divergence upon active faults that would localize geothermal heat and/or groundwater flow, both important components of the subglacial system.

# Basement topography and sediment thickness beneath Antarctica's Ross Ice Shelf imaged with airborne magnetic data

**M.D. Tankersley[1,2], H.J. Horgan[1], C.S. Siddoway[3], F. Caratori Tontini[2,4], K.J. Tinto[5]**

[1]Antarctic Research Centre, Victoria University of Wellington, Wellington, New Zealand
[2]GNS Science, Lower Hutt, New Zealand
[3]Colorado College, Colorado Springs, CO, USA
[4]University of Genova, Genova, Italy
[5]Lamont-Doherty Earth Observatory, Columbia University, Palisades, NY, USA

Tankersley ORCID: 0000-0003-4266-8554
Horgan ORCID: 0000-0002-4836-0078
Siddoway ORCID: 0000-0003-0478-6138
Caratori Tontini ORCID: 0000-0002-2000-416X
Tinto ORCID: 0000-0003-2558-2310

**Key Points:**

- Aeromagnetic analysis reveals basement topography beneath Antarctica's Ross Ice Shelf
- Sediment-filled extensional basins underlie the ice shelf, with continuity northward into the Ross Sea and southward to the Siple Coast
- Narrow, deep basins beneath Siple Coast suggest active rifting, with associated elevated geothermal heat flow and rapid GIA

Corresponding author: Matthew Tankersley, `matthew.tankersley@vuw.ac.nz`

## Abstract

New geophysical data from Antarctica's Ross Embayment illuminate the structure and subglacial geology of subsided continental crust beneath the Ross Ice Shelf. We use airborne magnetic data from the ROSETTA-Ice Project (2015-2019) to locate the basement-cover contact and map the extent of sedimentary basins. We delineate a broad, segmented high with thin (0-500 m) sedimentary cover which trends northward into the Ross Sea's Central High. Before subsiding below sea level, this feature likely facilitated early glaciation in the region and subsequently acted as a pinning point and ice flow divide. Flanking the high are wide basins, up to 3700 m deep, parallel with Ross Sea basins, which likely formed during Cretaceous-Neogene intracontinental extension. NW-SE basins beneath the Siple Coast grounding zone, by contrast, are narrow, deep, and elongate. They suggest tectonic divergence upon active faults that would localize geothermal heat and/or groundwater flow, both important components of the subglacial system.



## Plain Language Summary

The bedrock geology of Antarctica's southern Ross Embayment is concealed by 100s to 1000s of meters of glacial deposits, seawater, and the floating Ross Ice Shelf. Our research stripped away those layers to discover the shape of the consolidated bedrock below, which we refer to as the basement. We used the basement topography to obtain information about past continental landscapes of the Ross Embayment, and the manner of interaction of the basement – now subsided below sea level – with the Antarctic Ice Sheet. To do this, we used the contrast between non-magnetic sediments and magnetic basement rocks to map out the depth of the basement surface under the Ross Ice Shelf. Our primary data source was airborne measurements of the variation in Earth's magnetic field across the ice shelf, from flight lines spaced 10-km apart. We discovered contrasting basement characteristics on either side of the ice shelf, separated by an N-S trending basement high. The West Antarctic side basement features suggest active continental extension, which may localize high geothermal heat and dynamic responses of the earth to changes in the size of the Antarctic Ice Sheet. Our work addresses the connection between geology, tectonics, and glaciation in this region.


## 1 Introduction

Since the formation of Antarctic ice sheets in the Oligocene, the land surface of Antarctica has changed significantly (Paxman et al., 2019). For the Ross Embayment, this landscape evolution has been dominated by post-rift thermal subsidence following Cretaceous (Jordan et al., 2020) and Paleogene (Wilson & Luyendyk, 2009) continental extension, isostatic compensation of glacial erosion and sedimentation, and continued divergence across the western embayment (Granot et al., 2010). Accounting for these processes, topography reconstructions of Ross Embayment for past times show areas with elevation >500 m above sea level, including mountain ranges that hosted valley glaciers (e.g. De Santis, 1999; Sorlien et al., 2007). Now submerged, the Oligocene paleo-landscape of the Ross Sea sector was revealed by marine seismic data and drilling that penetrated the basement (e.g. Brancolini et al., 1995; Pérez et al., 2021) (Figure 1). This brought recognition that elevated topography of the Oligocene paleo-landscape played a role in the formation of the Antarctic Ice Sheet (DeConto & Pollard, 2003; Wilson et al., 2013), and subglacial topography still influences ice volume fluctuations caused by climate (Austermann et al., 2015; Colleoni et al., 2018).

The southern sector of Ross Embayment beneath the Ross Ice Shelf (RIS; area ∼480,000 km$^2$) is poorly resolved, by comparison, because the region is not easily accessible to conventional seismic or geophysical surveying. The RIS region is of high interest from the standpoint of regional ice sheet dynamics because its grounding zone (GZ) and pinning

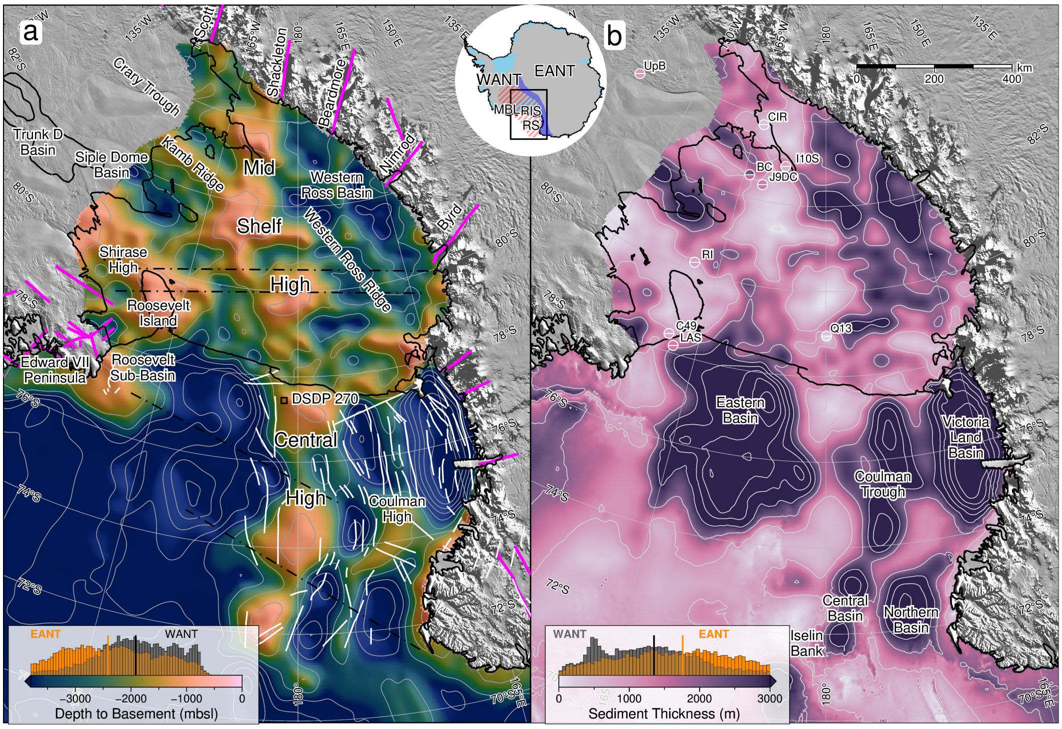


**Figure 1.** **(a)** Filtered depth to basement (magnetic for RIS, seismic elsewhere) contoured at 1 km. Pink lines are onshore mapped and inferred faults (Goodge, 2020; Siddoway, 2008; Ferraccioli et al., 2002). White lines are offshore faults (Salvini et al., 1997; Luyendyk et al., 2001; Chiappini et al., 2002). Dotted-dashed lines are OIB flight paths referred to here as 404.590, 404.650, 403.1, 403.3, from south to north. **(b)** Sediment thickness, contoured at 1 km, calculated as the difference between (a) and Bedmachine2 bathymetry (Morlighem et al., 2020) (Figure S1e). Previous basement-imaging RIS seismic surveys (Table S1) are plotted with upper and lower uncertainty ranges as circle halves, where reported. Colorbar histograms show data distribution for sub-RIS, separated into East and West Antarctic sides by a line down the center of the MSH (Figure S4). Vertical lines denote average values. Inset map shows figure location, ice shelves (blue), West Antarctic Rift System (hatched red), Transantarctic Mountains (dark blue), Abbreviations: WANT: West Antarctica, EANT: East Antarctica, MBL: Marie Byrd Land, RIS: Ross Ice Shelf, RS: Ross Sea. Shelf edge, grounding line and coastlines in black.

points buttress Antarctica's 2nd largest drainage basin (Tinto et al., 2019). Alongside the relevance of basement elevation for paleotopography, there is a need to delimit the extent of competent basement versus cover sediments. This is because the properties of the ice-bed interface influence the motion of the overriding ice by partitioning flow into sliding at the ice bed interface, deformation of the ice column, and deformation of the underlying substrate (e.g. Alley et al., 2004). Subglacial properties, including bed permeability and distribution of geothermal heat, also contribute to boundary conditions that influence ice sheet dynamics (e.g. Alley et al., 1986; Bell et al., 1998), control the resistance of GZ pinning points (Still et al., 2019), and promote the high flow velocities of West Antarctic ice streams (Blankenship et al., 2001; Tulaczyk et al., 1998). Here we present the first map of magnetic basement topography and sediment thickness for the southern Ross Embayment, developed using ROSETTA-Ice airborne magnetic data (Tinto et al., 2019). Our Werner deconvolution techniques reveal three major sedimentary basins and a broad basement ridge that separates crust of contrasting basement characteristics. This work provides the first holistic view of Ross Embayment crustal geology and structure at a scale appropriate to subglacial boundary conditions.

## 2 Data and Methods

We applied Werner deconvolution (Werner, 1953) to estimate the depth to the top of the magnetic crust along ROSETTA-Ice flight lines at 10-km spacing. The approach assumes that sediments and sedimentary rocks produce significantly lower amplitude magnetic anomalies than the underlying crystalline basement. Werner deconvolution can be performed on a 2D moving window of aeromagnetic line data by isolating anomalies and solving for their source parameters (Birch, 1984). The resulting solutions are non-unique; each observed magnetic anomaly can be solved by bodies at multiple locations and depths by varying the source's magnetic susceptibility and width. The result is a depth scatter of solutions (black dots in Figure 2). To estimate a basement surface, we filtered out the shallow solutions and clustered the remaining solutions (open circles in Figure 2) to produce a continuous distribution of points representing the top of the magnetic basement (orange crosses in Figure 2). The filtering was based on two parameters; Werner deconvolution window width (W) and a parameter (S) representing the product of the source's magnetic susceptibility and width. Clustering was performed by binning solutions (B, vertical grey lines in Figure 2) and retaining bins according to the count of solutions (C). See Text S1 for more details of magnetic data processing and Werner deconvolution.

We implemented a 2-step tuning process which ties our results to well-constrained ANTOSTRAT seismic basement in the Ross Sea (Brancolini et al., 1995). To facilitate this tie, we used Operation Ice Bridge (OIB) airborne magnetics data (Cochran et al., 2014) which flew over both the RIS and the Ross Sea. First, for a wide range of parameter values (W, S, B, and C) we calculated magnetic basement depth over the Ross Sea along OIB transect 403 and compared the result to ANTOSTRAT seismic basement depths (Figures 2&S2, Text S2). This allowed us to pick the parameter values which minimized the difference between the calculated aeromagnetic basement depths and ANTOSTRAT basement depths. With the optimized parameters, we calculated basement depths for OIB flight 404 (Figure S3) over the RIS. Using ROSETTA-Ice lines 590 & 650, coincident with OIB flight 404, we optimized the filtering and clustering parameters to minimize the difference between OIB and ROSETTA-Ice magnetic basement depths (Text S3). We then calculated magnetic basement for all ROSETTA-Ice flight lines and gridded the results (Figure S4, Text S4). Our resulting basement grid is the depth to the shallowest magnetic signal. Note that in some instances, such as igneous bodies intruded into sedimentary basin fill, Werner-determined solutions fall upon the crest of the intrusion, and the actual top of the crystalline basement could be at a deeper level. For intrusions of small lateral extent, these solutions will be excluded by our filter process, and the deep basement sources will still be recognized. Results from this study are merged with ANTOSTRAT data (Brancolini et al., 1995, Text S4) and smoothed with an 80 km Gaussian filter (Figure 1a) to match the characteristic wavelengths of the Ross Sea basement. The combined grid was then subtracted from Bedmachine2 bathymetry (Morlighem et al., 2020) (Figure S1e), which contains ROSETTA-Ice sub-RIS modeled bathymetry (Tinto et al., 2019), to obtain the sediment thickness distribution for the entire Ross Embayment (Figure 1b).

We used basement features and geophysical anomaly patterns to infer regional scale faults beneath the RIS. Criteria used to locate faults include 1) high relief on the magnetic basement surface, 2) linear trends that transect zones of shallow basement, 3) high gradient gravity anomalies and 4) large contrasts in modeled sediment thickness. We display the inferred faults upon a base map of crustal stretching factors ($\beta$-factor; the ratio of crustal thickness before and after extension, Figure 3a), using an initial crustal thick-

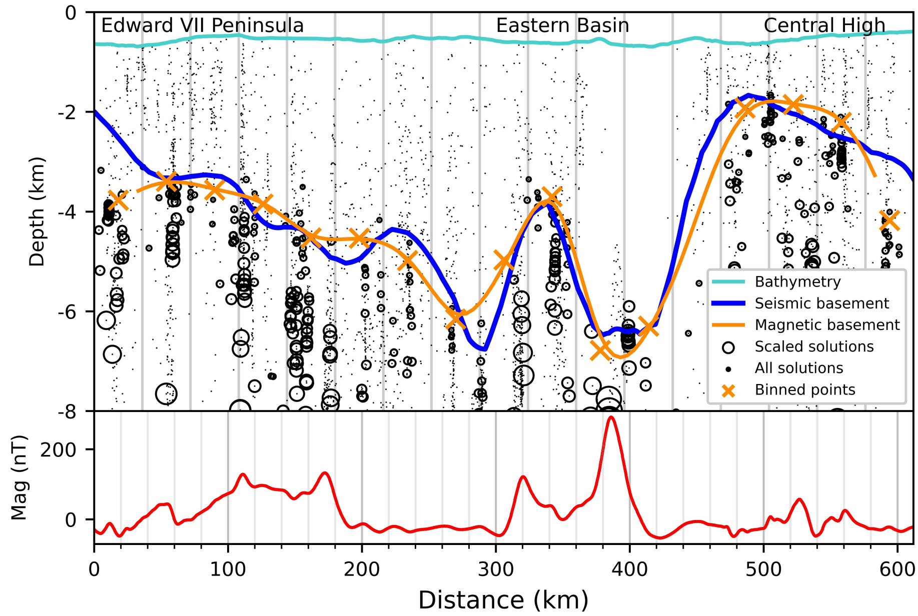


**Figure 2.** Werner deconvolution solutions for Operation Ice Bridge (OIB) flight 403 over the Ross Sea (line here termed 403-1, location Figure 1a). Bathymetry from Bedmap2 (Fretwell et al., 2013). Seismic basement from ANTOSTRAT (Brancolini et al., 1995). Filtering and clustering are described in Methods and Text S2. Circles are scaled to parameter S. Mean absolute difference between magnetic basement (orange line) and seismic basement (blue line) is 332 m.

ness of 38 km (Müller et al., 2007), a continent-wide Moho model (An et al., 2015), and our basement surface as the top of the crust (Text S5).

## 3 Results

The basement depths and sediment thickness grids, calculated using the greater data density afforded by ROSETTA-Ice and OIB surveys, provide new resolution of the sub-RIS upper crustal structure. An almost continuous drape of sediment covers the RIS region (Figure 1b), with <1% of the area having <100 m of sediment cover. Our tie between ROSETTA-Ice magnetic basement and Ross Sea seismic is achieved using OIB magnetics data to bridge the gap. The tie between OIB magnetic basement and Ross Sea seismic basement (Figures 2&S2) gives a mean absolute difference of 970 m. The tie between OIB and ROSETTA-Ice magnetic basement (Lines 590&650, Figure S3) give a mean absolute difference of 560 m. On the ice shelf, eight seismic estimates of sediment thickness, independent from our study, gives a mean absolute difference of 470 m from our results (Table S1 & Figure 1b). Three seismic profiles on the RIS report up to several kilometers of sediment, in general accordance with our results (Stern et al., 1991; ten Brink et al., 1993; Beaudoin et al., 1992).

Prominent beneath the midline of the RIS is a broad NNW-SSE trending basement ridge, here-called the Mid-Shelf High (MSH). The MSH is segmented into three blocks, separated by narrow orthogonal valleys. These blocks comprise most of the shallowest (<700 mbsl) sub-RIS basement, with several regions having <50 m sedimentary cover. The southern MSH abuts the TAM in the vicinity of Shackleton Glacier. At the regional scale, basement contrasts are apparent on either side of the MSH, with average basement depths of ∼-2410 mbsl on the East Antarctic side, compared to ∼-1910 mbsl on the West Antarctic side (Figure 1a colorbar). Sedimentary fill is ∼400 m greater and more uniformly distributed on the East Antarctic side than the West Antarctic side (Figure 1b colorbar).

There is a single broad and deep basin (200 x 600 km) between the MSH and the TAM, here termed the Western Ross Basin (Figure 1a). The Western Ross Basin parallels the TAM and contains a narrow NW-SE trending ridge that runs the full length of the basin. The linear basement ridge, here termed the Western Ross Ridge, displays ∼1500 m structural relief above the basement sub-basins on either side. The TAM-side basin has the highest-observed sub-RIS basement depths of 4500 mbsl, accommodating sediments that are up to 3800 m thick.

Bordering the MSH on the east, an elongate NW-SE trending basin runs from the RIS calving front to the Siple Coast GZ (Figure 1a). It is segmented by two gentle rises, then deepens abruptly beneath Siple Dome where we discover a 150x200 km depocenter reaching basement depths up to 4000 mbsl, with sediments up to 3700 m thick. We refer to this depocenter as Siple Dome Basin (SDB). SDB's east margin is formed by a basement high that trends southward from Roosevelt Island. Here termed the Shirase High, the feature rises to its shallowest point at the GZ, where its sedimentary cover is less than 100 m. A second deep, narrow basin (50x200 km in dimension) is found along the north margin of Crary Ice Rise, separated from the SDB by an NW-SE ridge (Kamb Ridge) underlying Kamb Ice Stream. The basin, here termed Crary Trough, contains sediments 1800-2700 m thick and the basement reaches depths of 3200 mbsl. At the southernmost region of the RIS is an additional depocenter, up to 2000 m thick, beneath Whillans Ice Stream (location in Figure 3a).

With the criteria outlined in Methods, we identified a series of likely locations for active and inactive sub-RIS faults (Figure 3a). We find active faults are concentrated on the West Antarctic side, where basement basins are narrow, linear, and coincide with high-gradient gravity anomalies (Figure S1a). Inactive normal and strike-slip faults are inferred between the shallow blocks of the MSH, and inline with Transantarctic Mountain (TAM) outlet glacier faults. $\beta$-factors show a distinct signature on the east vs west side of the MSH, with the TAM side showing high $\beta$-factors (average 1.99) with low variability while the West Antarctic side has lower $\beta$-factors (average 1.82), with localized zones of higher values (up to 2.1) (Figure 3a).

## 4 Discussion

Sub-RIS sedimentary basins align with and show lateral continuity with (from east to west, Figure 1) the Ross Sea's Roosevelt Sub-Basin, Eastern Basin, Coulman Trough, and Victoria Land Basin. The MSH forms the prominent southward continuation of the Ross Sea's Central High (CH). At the southern RIS margin, the narrow SDB has continuity with the previously identified Trunk D Basin (Bell et al., 2006) (Figure 1a). These regional continuations display sub-RIS basement features within the context of the Ross Sea (e.g. Cooper et al., 1995) and central West Antarctica (e.g. Bell et al., 2006) crustal structure.

### 4.1 West Antarctic Rift System extensional basins

Here we show the first geophysically constrained evidence of large-scale continental rifting beneath the RIS (Figure 3). Our basement map shows that rift basins of the eastern Ross Sea continue southward beneath the ice shelf as far as the Siple Coast, while those of the western Ross Sea terminate along the MSH. The Western Ross Basin has a configuration similar to the western Ross Sea rift basins in that it is a broad and deep basin, separated into distinct depocenters by a low relief ridge. The deeper of the depocenters is on the TAM side of the ridge and coincides with a narrow gravity low (Figure S1a). These similarities to the western Ross Sea basins, and the parallelism in trend between them, suggest these features are the sub-RIS continuations of the Coulman Trough, Coulman High, and the Victoria Land Basin, likely sharing a common tectonic origin. These sub-RIS basins terminate against the southern segment of the MSH (Figure 1a; along 180° meridian). The basin margins are likely fault-controlled (Figure 3a), as in the Ross Sea (e.g. Salvini et al., 1997) (Figure 1a, white lines).

The TAM-side of the Western Ross Basin likely marks and bounds the southward continuation of the Terror Rift, a southward-narrowing graben (Sauli et al., 2021) formed due to Neogene oceanic spreading in the Adare Trough (Henrys et al., 2007; Granot et al., 2010). This Neogene event caused extension in the Ross Sea and is inferred to transition into strike-slip under the RIS (Granot & Dyment, 2018). We infer that the southern limit of the Western Ross Basin, along the MSH, corresponds to a transfer fault between sectors of crust extended to different degrees (Figure 3a). The structure passes southward beneath Shackleton Glacier, which occupies a fault-controlled trough and crustal boundary (Borg et al., 1990).

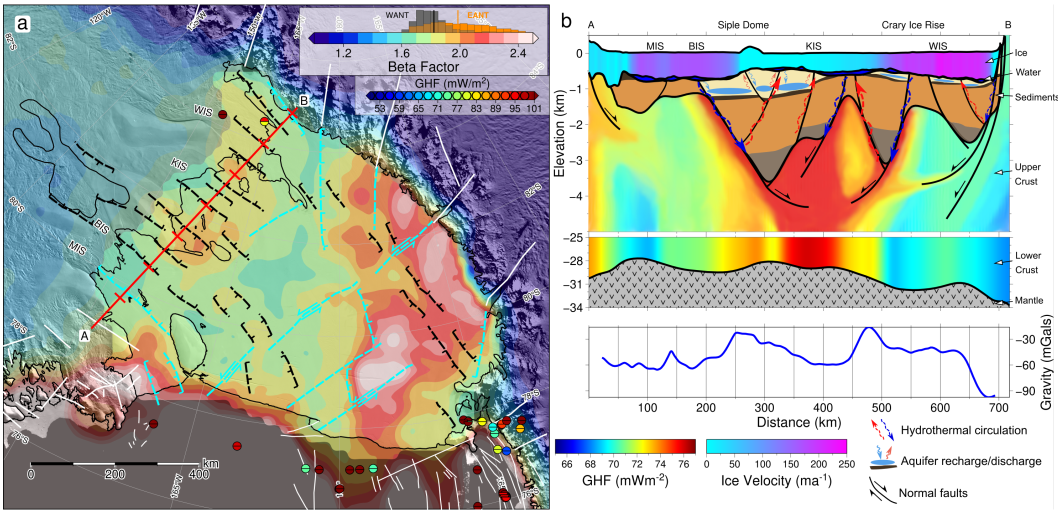


**Figure 3.** Tectonic interpretation of the sub-RIS. **(a)** $\beta$ stretching factors (Text S5). Colorbar histogram shows east vs west data distribution, same as Figure 1. White faults and black basin outline same as Figure 1a, black and cyan dashed lines indicate inferred active and inactive faults, respectively, with kinematics shown. GHF point measurements plotted with upper and lower uncertainty ranges as circle halves, if reported (Burton-Johnson et al., 2020). Profile location in red, with 100 km ticks. **(b)** Siple Coast cross-section from A-B. Ice surface, ice base, and bathymetry from Bedmachine2 (Morlighem et al., 2020). Basement surface merged to bed outside of data coverage. Ice colored by velocity (Mouginot et al., 2019). Sediment layer shows interpreted faults, offset beds, aquifers, and water transport. Upper crust shows theoretical GHF guided by inferred faults and GHF models (Burton-Johnson et al., 2020), which color the lower crust, from Moho (Shen et al., 2018) to –25km. Lower panel shows ROSETTA-Ice gravity. Abbreviations: MIS: MacAyeal Ice Stream, BIS: Bindschadler Ice Stream, KIS: Kamb Ice Stream, WIS: Whillans Ice Stream.

Beneath the GZ at the southeastern RIS margin, ridges and narrow basins define a prominent NW-SE trend. The narrow, deep basin profiles, thick sediments, and strong definition of high-gradient gravity anomalies (Figure S1a) suggest the presence of NW-SE-oriented normal faults accommodating active divergent tectonics in this domain. Our Siple Coast cross-section (Figure 3b) displays these inferred faults associated with the SDB and Crary Trough formation. Local gravity surveys have imaged portions of the basin-bounding faults, with contrasting sediment thicknesses indicating up to 600 m of throw along the Whillans Ice Stream flank (Muto et al., 2013) (Figure 3a) and J9DC (Greischar et al., 1992) (Figure 1b). The sharp definition of Crary Trough and Siple Dome Basin signifies that this domain of Neogene extension is distinct from the southward-narrowing mid-Cenozoic divergence recognized for the Ross Sea (e.g. Cande et al., 2000; Davey et al., 2006). There is continuity from the narrow SDB into the previously identified Trunk D Basin (Bell et al., 2006) (Figure 1a) indicating the significant areal extent of the active tectonic domain into West Antarctica. A decrease in $\beta$-factors from the well-constrained RIS into West Antarctica, where sediment basins haven't been removed from the crustal thickness calculation, shows that knowledge of basement topography significantly changes $\beta$-factor estimates.

### 4.2 Solid-Earth-cryosphere interactions

Glacioisostatic adjustment following deglaciation in a region such as the Siple Coast, with low mantle viscosities (Whitehouse et al., 2019) and a landward-deepening bed (Adhikari et al., 2014), results in a negative feedback that can stabilize the ice sheet (Coulon et al., 2021). This rebound-driven ice sheet re-advance has been suggested for the region during the Holocene (Kingslake et al., 2018) and is dependent on mantle viscosity and its variability (Lowry et al., 2020). Active graben-bounding faults, as suggested here, and the elevated geotherm from recent extension would result in the rapid crustal responses to ice volume changes.

Groundwater reservoirs within sedimentary basins are estimated to store up to half of subglacial water, which enables the fast flow of the Siple Coast ice streams (Christoffersen et al., 2014). As this water is discharged or recharged, via fault damage zones (Jolie et al., 2021), it concentrates geothermal heat flux (GHF), drawing it up to the ice-bed interface or suppressing it to lower depths (Gooch et al., 2016). This vertical groundwater flow is modulated by pressure from the overriding ice sheets (Piotrowski, 2006; Siegert et al., 2018). High heat flux has been observed at one of the depocenters we defined at the GZ beneath Whillans Ice Stream (Fisher et al., 2015) (Figure 3a) and estimated seismologically along the Siple Coast (Shen et al., 2020) (Figure 3b). The steeply dipping normal faults and the potential basinal aquifers likely affect the localization and magnitude of GHF and subglacial water fluxes (Figure 3b).

### 4.3 Central High - Mid-Shelf High

Based on contrast in crustal characteristics, including magnetic anomalies, Tinto et al. (2019) suggest a mid-Ross Embayment north-south trending major geologic boundary separating crust of East and West Antarctic affinity. Geological substantiation comes from basement rock samples recovered from the CH at DSDP 270 (Ford & Barrett, 1975), and at Iselin Bank (Mortimer et al., 2011) (Figure 1), which have lithologic affinities to the TAM. This N-S boundary is coincident through the entire embayment with the CH-MSH. The distinct geologic properties on either side of the MSH related to West versus East Antarctic type crust have likely controlled the respective responses to West Antarctic Rift System extension (Tinto et al., 2019). High and homogeneous $\beta$-factors on the TAM-side indicate distributed crustal extension, while the West Antarctic side's $\beta$-factors are representative of localized intense rifting within a region of generally less thinned crust (Figure 3a). The greater amount of extension on the East Antarctic side is corroborated with the deeper bathymetry (Tinto et al., 2019) and deeper basement (Figure 1a).

Under the RIS, this CH-MSH feature trends southward from the calving front to the TAM. At the intersection with the TAM, the western edge of the high aligns with Shackleton Glacier which occupies a major fault separating the distinct geologic domains of the central and southern TAM (Borg et al., 1990; Paulsen et al., 2004; Miller et al., 2010). Previous workers noted that the Shackleton Glacier Fault trends into a 250-km long fault that passes from the south side of the TAM (Drewry, 1972) into a prominent magnetic lineament at the South Pole (Studinger et al., 2006). This N-S sequence of structures from Shackleton Glacier to the South Pole may be an expression of the East Antarctic craton margin or a major intracontinental transform (Studinger et al., 2006) (Figure 3a). The spatial correspondence of the East-West Antarctic geologic boundary, the N-S series of linear features, and the prominent basement highs suggest the CH-MSH is a major tectonic feature which through tectonic inheritance has influenced the rift architecture and development of Ross Embayment (Corti et al., 2007).

Paleotopographic reconstructions of the Late Paleogene depict a proto-Ross Embayment divided by a long, narrow mountain range, emergent above sea level (Paxman et al., 2019; Wilson et al., 2012), that hosted alpine glaciers and small ice caps (De Santis et al., 1995; De Santis, 1999). These represent the initial glacial stage in the region, and, once established, were the centers from which continental ice expanded to the outer Ross Sea continental shelf (Bart & De Santis, 2012). As the CH subsided by up to 500 m through the Neogene (Leckie, 1983) it submerged below sea level, but remained a bathymetric high until the mid-Miocene, before sedimentary deposits covered it (De Santis et al., 1995). The geophysical similarities and continuity between the Ross Sea's CH and the RIS's MSH imply a similar glaciation and subsidence history for the RIS region as for the Ross Sea. The terrestrial/alpine stage for the MSH helps to explain the region's potential to hold the late Oligocene's larger-than-modern ice volumes (Wilson et al., 2013; Pekar et al., 2006). Analysis of subglacial sediment identified a major ice flow divide between East and West Antarctic ice since the Last Glacial Maximum (Li et al., 2020; Licht et al., 2014; Coenen et al., 2019). These findings highlight the CH-MSH as important features for both Oligocene ice sheet development and the subsequent evolution of the ice sheet and ice shelf to the present day.

### 4.4 Thermal subsidence and sedimentation

Incorporating the updated basement basin extents and geometries into post-rift thermal subsidence modeling will enable better constrained paleotopographic reconstructions. A model for post-Eocene thermal subsidence following rifting of the West Antarctic Rift System predicts sub-RIS subsidence values based on gravity-derived basin geometries, uniform $\beta$-factors, and instantaneous extension ages based on plate-circuit data (Wilson et al., 2012; Paxman et al., 2019). They predict a relatively uniform southward decrease in subsidence for the sub-RIS continuation of the Eastern Basin. Instead, we discovered the narrow, deep SDB beneath the GZ, trending directly into Trunk D Basin. The basins' geometry suggests active structures and tectonic subsidence (Figure 3b). Consequently, the paleotopography of Siple Dome should restore to a higher elevation than was determined in paleogeographic reconstructions (Wilson et al., 2012; Paxman et al., 2019).

Our sediment thickness comparison with past models (Decesari et al., 2007) shows the majority of the sub-RIS contains more sediment than previously estimated (Figure S1f). This finding has implications for surface elevation changes due to sediment deposition. According to Paxman et al. (2019), sediment loading in Ross Embayment caused up to 2 km of isostatic response via subsidence in major depocenters since the Eocene, with the degree of subsidence diminishing southward from the Ross Sea to the Siple Coast. Our improved sub-RIS sediment thickness estimates, of up to 4 km along the Siple Coast and Western Ross Basin, imply a late Eocene-Oligocene paleotopography higher than today's. Depending on the age of the sediment, reconstructions for parts of the sub-RIS are therefore likely to be too low.

## 5 Conclusions

Here we present a depth to magnetic basement for the Ross Ice Shelf from Werner deconvolution of airborne magnetics data. The magnetic basement derived for the RIS is tied to acoustic basement of the Ross Sea, providing the first synthetic view of Ross Embayment crustal structure. Subtracting a bathymetry model (Tinto et al., 2019) we obtain sediment thickness distribution for the region. With these two grids and the magnetics data, we identify the likely positions for crustal faults, basement highs likely to function as pinning points at ice sheet high stands, and sites where the localization of geothermal heat or subglacial groundwater may affect boundary conditions. Sub-RIS sedimentary basins have continuity with Ross Sea basins to the north, and the prominent Mid-Shelf High trends northward into the Ross Sea's Central High. The High separates crust of contrasting geophysical character, affected by different stages of continental extension. The Mid-Shelf High was likely subaerial in the Oligocene, facilitating the formation of ice caps in early Antarctic glaciation, and subsequently acted as an ice flow divide between East and West Antarctic Ice Sheets. Newly identified narrow, linear, and deep sedimentary basins provide evidence for active extension beneath the Siple Coast grounding zone. The thinned crust likely experiences elevated geothermal heat flow promoting the formation of subglacial water. Fault motions may accommodate a rapid glacioisostatic response to ice sheet volume changes along the RIS's Siple Coast. Groundwater storage and transport to the ice-bed interface are likely controlled by permeable basin fill and fault-controlled basement interfaces, with possible localization of geothermal heat. Our work contributes critical information about Ross Embayment subglacial boundary conditions that arise from an interplay of geology, tectonics, and glaciation.

## Acknowledgments

Funding support from the New Zealand Ministry of Business and Innovation and Employment through the Antarctic Science Platform contract (ANTA1801) Antarctic Ice Dynamics Project (ASP-021-01) and from the National Science Foundation (1443497 and 1443534). Figures were created using GMT6/PyGMT (Wessel et al., 2019; Uieda et al., 2021), with a script adapted from Venturelli et al. (2020). Grounding line, coastline, and background imagery in figures are from Rignot and Scheuchl (2016); Rignot et al. (2011, 2014); Scambos et al. (2007). Geosoft Oasis Montaj™ was used for magnetics processing and Werner deconvolution. ROSETTA-Ice and OIB magnetics data are available from https://pgg.ldeo.columbia.edu/data. Results from this study are available to download from https://figshare.com/s/ceea920c01073fff302b. We thank Tim Stern, Simon Lamb, and Lara Pérez for useful discussions, and the ROSETTA-Ice team for data collection and processing.

## References

Adhikari, S., Ivins, E. R., Larour, E., Seroussi, H., Morlighem, M., & Nowicki, S. (2014). Future Antarctic bed topography and its implications for ice sheet dynamics. *Solid Earth*, *5*(1), 569–584. http://doi.org/10.5194/se-5-569-2014

Alley, R. B., Anandakrishnan, S., Dupont, T. K., & Parizek, B. R. (2004). Ice streams—fast, and faster? *Comptes Rendus Physique*, *5*(7), 723–734. http://doi.org/10.1016/j.crhy.2004.08.002

Alley, R. B., Blankenship, D. D., Bentley, C. R., & Rooney, S. T. (1986). Deformation of till beneath ice stream B, West Antarctica. *Nature*, *322*(6074), 57–59. http://doi.org/10.1038/322057a0

An, M., Wiens, D. A., Zhao, Y., Feng, M., Nyblade, A. A., Kanao, M., … Lévêque, J.-J. (2015). S-velocity model and inferred Moho topography beneath the Antarctic Plate from Rayleigh waves: Antarctic S-velocities and Moho. *Journal of Geophysical Research: Solid Earth*, *120*(1), 359–383. http://doi.org/10.1002/2014JB011332

Austermann, J., Pollard, D., Mitrovica, J. X., Moucha, R., Forte, A. M., DeConto, R. M., … Raymo, M. E. (2015). The impact of dynamic topography change on Antarctic ice sheet stability during the mid-Pliocene warm period. *Geology*, *43*(10), 927–930. http://doi.org/10.1130/G36988.1

Bart, P., & De Santis, L. (2012). Glacial intensification during the Neogene: a review of seismic stratigraphic evidence from the Ross Sea, Antarctica, continental shelf. *Oceanography*, *25*(3), 166–183. http://doi.org/10.5670/oceanog.2012.92

Beaudoin, B. C., ten Brink, U. S., & Stern, T. A. (1992). Characteristics and processing of seismic data collected on thick, floating ice: Results from the Ross Ice Shelf, Antarctica. *Geophysics*, *57*(10), 1359–1372. http://doi.org/10.1190/1.1443205

Bell, R. E., Blankenship, D. D., Finn, C. A., Morse, D. L., Scambos, T. A., Brozena, J. M., & Hodge, S. M. (1998). Influence of subglacial geology on the onset of a West Antarctic ice stream from aerogeophysical observations. *Nature*, *394*(6688), 58–62. http://doi.org/10.1038/27883

Bell, R. E., Studinger, M., Karner, G., Finn, C. A., & Blankenship, D. D. (2006). Identifying major sedimentary basins beneath the West Antarctic Ice Sheet from aeromagnetic data analysis. In D. K. Fütterer, D. Damaske, G. Kleinschmidt, H. Miller, & F. Tessensohn (Eds.), *Antarctica* (pp. 117–121). Berlin/Heidelberg: Springer-Verlag. http://doi.org/10.1007/3-540-32934-X_13

Birch, F. (1984). Bedrock depth estimates from ground magnetometer profiles Werner deconvolution. *Ground Water*, *22*(4), 427–432. https://doi.org/10.1111/j.1745-6584.1984.tb01413.x

Blankenship, D. D., Morse, D. L., Finn, C. A., Bell, R. E., Peters, M. E., Kempf,

S. D., ... Brozena, J. M. (2001). Geologic controls on the initiation of rapid basal motion for West Antarctic Ice Streams: a geophysical perspective including new airborne radar sounding and laser altimetry results. In R. B. Alley & R. A. Bindschadler (Eds.), *Antarctic Research Series* (pp. 105–121). Washington, D. C.: American Geophysical Union. https://doi.org/10.1029/AR077p0105

Borg, S. G., Depaolo, D. J., & Smith, B. M. (1990). Isotopic structure and tectonics of the central Transantarctic mountains. *Journal of Geophysical Research*, *95*(B5), 6647. https://doi.org/10.1029/JB095iB05p06647

Brancolini, G., Busetti, M., Marchetti, A., Santis, L. D., Zanolla, C., Cooper, A. K., ... Hinze, K. (1995). Descriptive text for the seismic stratigraphic atlas of the Ross Sea, Antarctica. In A. K. Cooper, P. F. Barker, & G. Brancolini (Eds.), *Geology and Seismic Stratigraphy of the Antarctic Margin* (Vol. 68, pp. A271–A286). Washington, D. C.: American Geophysical Union. https://doi.org/10.1002/9781118669013.app1

Burton-Johnson, A., Dziadek, R., & Martin, C. (2020). Geothermal heat flow in Antarctica: current and future directions. *The Cryosphere Discussions*, 1–45. https://doi.org/10.5194/tc-2020-59

Cande, S. C., Stock, J. M., Müller, R. D., & Ishihara, T. (2000). Cenozoic motion between East and West Antarctica. *Nature*, *404*(6774), 145–150. https://doi.org/10.1038/35004501

Chiappini, M., Ferraccioli, F., Bozzo, E., & Damaske, D. (2002). Regional compilation and analysis of aeromagnetic anomalies for the Transantarctic Mountains–Ross Sea sector of the Antarctic. *Tectonophysics*, *347*(1-3), 121–137. https://doi.org/10.1016/S0040-1951(01)00241-4

Christoffersen, P., Bougamont, M., Carter, S. P., Fricker, H. A., & Tulaczyk, S. (2014). Significant groundwater contribution to Antarctic ice streams hydrologic budget. *Geophysical Research Letters*, *41*(6), 2003–2010. https://doi.org/10.1002/2014GL059250

Cochran, J. R., Burton, B., Frearson, N., & Tinto, K. (2014). IceBridge Scintrex CS-3 Cesium magnetometer L1B geolocated magnetic anomalies, version 2. [Line 403, 404]. *Boulder, Colorado USA. NASA National Snow and Ice Data Center Distributed Active Archive Center*. https://doi.org/10.5067/OY7C2Y61YSYW

Coenen, J. J., Scherer, R. P., Baudoin, P., Warny, S., Castañeda, I. S., & Askin, R. (2019). Paleogene marine and terrestrial development of the West Antarctic Rift System. *Geophysical Research Letters*, *47*(3). https://doi.org/10.1029/2019GL085281

Colleoni, F., De Santis, L., Montoli, E., Olivo, E., Sorlien, C. C., Bart, P. J., ... Prato, S. (2018). Past continental shelf evolution increased Antarctic ice sheet sensitivity to climatic conditions. *Scientific Reports*, *8*(1), 11323. https://doi.org/10.1038/s41598-018-29718-7

Cooper, A. K., Barker, P. F., & Brancolini, G. (Eds.). (1995). *Geology and seismic stratigraphy of the Antarctic margin* (No. v. 68). Washington, D.C: AGU. https://doi.org/10.1029/AR068

Corti, G., van Wijk, J., Cloetingh, S., & Morley, C. K. (2007). Tectonic inheritance and continental rift architecture: Numerical and analogue models of the East African Rift system. *Tectonics*, *26*(6), 1–13. https://doi.org/10.1029/2006TC002086

Coulon, V., Bulthuis, K., Whitehouse, P. L., Sun, S., Haubner, K., Zipf, L., & Pattyn, F. (2021). Contrasting response of West and East Antarctic Ice Sheets to glacial isostatic adjustment. *Journal of Geophysical Research: Earth Surface*, *126*(7). https://doi.org/10.1029/2020JF006003

Crary, A. P. (1961). Marine-sediment thickness in the eastern Ross Sea area, Antarctica. *Geological Society of America Bulletin*, *72*(5), 787. https://doi.org/10

.1130/0016-7606(1961)72[787:MTITER]2.0.CO;2
Davey, F. J., Cande, S. C., & Stock, J. M. (2006). Extension in the western Ross Sea region-links between Adare Basin and Victoria Land Basin. *Geophysical Research Letters*, *33*(20), 1–5. https://doi.org/10.1029/2006GL027383
Decesari, R. C., Wilson, D. S., Luyendyk, B., & Faulkner, M. (2007). Cretaceous and Tertiary extension throughout the Ross Sea, Antarctica. *U.S. Geological Survey and the National Academies*, *10th International Symposium on Antarctic Earth Sciences*, 1–6. https://doi.org/10.3133/of2007-1047.srp098
DeConto, R. M., & Pollard, D. (2003). A coupled climate–ice sheet modeling approach to the Early Cenozoic history of the Antarctic ice sheet. *Palaeogeography, Palaeoclimatology, Palaeoecology*, *198*(1-2), 39–52. https://doi.org/10.1016/S0031-0182(03)00393-6
De Santis, L. (1999). The Eastern Ross Sea continental shelf during the Cenozoic: implications for the West Antarctic ice sheet development. *Global and Planetary Change*, *23*(1-4), 173–196. https://doi.org/10.1016/S0921-8181(99)00056-9
De Santis, L., Anderson, J. B., Brancolini, G., & Zayatz, I. (1995). Seismic record of late Oligocene through Miocene glaciation on the central and eastern continental shelf of the Ross Sea. In A. K. Cooper, P. F. Barker, & G. Brancolini (Eds.), *Antarctic Research Series* (pp. 235–260). Washington, D. C.: American Geophysical Union. https://doi.org/10.1029/AR068p0235
Drewry, D. (1972). Subglacial morphology between the Transantarctic Mountains and the South Pole. In R. Adie (Ed.), *Antarctic Geology and Geophysics* (Vol. 1, pp. 693–703). Oslo: International Union of Geological Science. https://doi.org/10.26153/tsw/2786
Ferraccioli, F., Bozzo, E., & Damaske, D. (2002). Aeromagnetic signatures over western Marie Byrd Land provide insight into magmatic arc basement, mafic magmatism and structure of the Eastern Ross Sea Rift flank. *Tectonophysics*, *347*, 139–165. https://doi.org/10.1016/S0040-1951(01)00242-6
Fisher, A. T., Mankoff, K. D., Tulaczyk, S. M., Tyler, S. W., Foley, N., & and the WISSARD Science Team. (2015). High geothermal heat flux measured below the West Antarctic Ice Sheet. *Science Advances*, *1*, 1–9. https://doi.org/10.1126/sciadv.1500093
Ford, A., & Barrett, P. J. (1975). *Basement rocks of the south-central Ross Sea, site 270, DSDP leg 28* (Tech. Rep.). College Station, TX, United States: Texas A & M University, Ocean Drilling Program. https://doi.org/10.2973/dsdp.proc.28.130.1975
Fretwell, P., Pritchard, H. D., Vaughan, D. G., Bamber, J. L., Barrand, N. E., Bell, R. E., … Zirizzotti, A. (2013). Bedmap2: improved ice bed, surface and thickness datasets for Antarctica. *The Cryosphere*, *7*(1), 375–393. https://doi.org/10.5194/tc-7-375-2013
Gooch, B. T., Young, D. A., & Blankenship, D. D. (2016). Potential groundwater and heterogeneous heat source contributions to ice sheet dynamics in critical submarine basins of East Antarctica. *Geochemistry, Geophysics, Geosystems*, *17*(2), 395–409. https://doi.org/10.1002/2015GC006117
Goodge, J. W. (2020). Geological and tectonic evolution of the Transantarctic Mountains, from ancient craton to recent enigma. *Gondwana Research*, *80*, 50–122. https://doi.org/10.1016/j.gr.2019.11.001
Granot, R., Cande, S. C., Stock, J. M., Davey, F. J., & Clayton, R. W. (2010). Postspreading rifting in the Adare Basin, Antarctica: Regional tectonic consequences. *Geochemistry, Geophysics, Geosystems*, *11*(8), 1–29. https://doi.org/10.1029/2010GC003105
Granot, R., & Dyment, J. (2018). Late Cenozoic unification of East and West Antarctica. *Nature Communications*, *9*(1), 3189. https://doi.org/10.1038/s41467-018-05270-w

Greischar, L. L., Bentley, C. R., & Whiting, L. R. (1992). An analysis of gravity measurements on the Ross Ice Shelf, Antarctica. In *Contributions to Antarctic Research III* (pp. 105–155). American Geophysical Union (AGU). https://doi.org/10.1029/AR057p0105

Henrys, S., Wilson, T., Whittaker, J., Fielding, C., Hall, J., & Naish, T. (2007). Tectonic history of the mid-Miocene to present southern Victoria Land Basin, inferred from seismic stratigraphy in McMurdo Sound. *U.S. Geological Survey and the National Academies*. (Series: Open-File Report) https://doi.org/10.3133/of2007-1047.srp049

Jolie, E., Scott, S., Faulds, J., Chambefort, I., Axelsson, G., Gutiérrez-Negrín, L. C., ... Zemedkun, M. T. (2021). Geological controls on geothermal resources for power generation. *Nature Reviews Earth & Environment*, *2*(5), 324–339. https://doi.org/10.1038/s43017-021-00154-y

Jordan, T. A., Riley, T. R., & Siddoway, C. S. (2020). The geological history and evolution of West Antarctica. *Nature Reviews Earth & Environment*, *1*, 117–133. https://doi.org/10.1038/s43017-019-0013-6

Kingslake, J., Scherer, R. P., Albrecht, T., Coenen, J., Powell, R. D., Reese, R., ... Whitehouse, P. L. (2018). Extensive retreat and re-advance of the West Antarctic Ice Sheet during the Holocene. *Nature*, *558*(7710), 430–434. https://doi.org/10.1038/s41586-018-0208-x

Leckie, F. M. (1983). Late Oligocene-early Miocene glacial record of the Ross Sea, Antarctica: Evidence from DSDP Site 270. *Geology*, *11*, 578–582. https://doi.org/10.1130/0091-7613(1983)11⟨578:LOMGRO⟩2.0.CO;2

Li, X., Zattin, M., & Olivetti, V. (2020). Apatite fission track signatures of the Ross Sea ice flows during the Last Glacial Maximum. *Geochemistry, Geophysics, Geosystems*, *21*(10), 1–21. https://doi.org/10.1029/2019GC008749

Licht, K. J., Hennessy, A. J., & Welke, B. M. (2014). The U-Pb detrital zircon signature of West Antarctic ice stream tills in the Ross embayment, with implications for Last Glacial Maximum ice flow reconstructions. *Antarctic Science*, *26*(6), 687–697. https://doi.org/10.1017/S0954102014000315

Lindeque, A., Gohl, K., Wobbe, F., & Uenzelmann-Neben, G. (2016). Preglacial to glacial sediment thickness grids for the Southern Pacific Margin of West Antarctica: Preglacial, transitional and full glacial isopach maps, West Antarctica. *Geochemistry, Geophysics, Geosystems*, *17*(10), 4276–4285. https://doi.org/10.1002/2016GC006401

Lowry, D. P., Golledge, N. R., Bertler, N. A., Jones, R. S., McKay, R., & Stutz, J. (2020). Geologic controls on ice sheet sensitivity to deglacial climate forcing in the Ross Embayment, Antarctica. *Quaternary Science Advances*, *1*, 1–17. https://doi.org/10.1016/j.qsa.2020.100002

Luyendyk, B., Sorlien, C. C., Wilson, D. S., Bartek, L. R., & Siddoway, C. S. (2001). Structural and tectonic evolution of the Ross Sea rift in the Cape Colbeck region, Eastern Ross Sea, Antarctica. *Tectonics*, *20*(6), 933–958. https://doi.org/10.1029/2000TC001260

Miller, S. R., Fitzgerald, P. G., & Baldwin, S. L. (2010). Cenozoic range-front faulting and development of the Transantarctic Mountains near Cape Surprise, Antarctica: Thermochronologic and geomorphologic constraints. *Tectonics*, *29*(1), 1–21. https://doi.org/10.1029/2009TC002457

Mooney, W. D., Laske, G., & Masters, T. G. (1998). CRUST 5.1: A global crustal model at $5^{\circ} \times 5^{\circ}$. *Journal of Geophysical Research: Solid Earth*, *103*(B1), 727–747. https://doi.org/10.1029/97JB02122

Morlighem, M., Rignot, E., Binder, T., Blankenship, D., Drews, R., Eagles, G., ... Young, D. A. (2020). Deep glacial troughs and stabilizing ridges unveiled beneath the margins of the Antarctic ice sheet. *Nature Geoscience*, *13*(2), 132–137. https://doi.org/10.1038/s41561-019-0510-8

Mortimer, N., Palin, J., Dunlap, W., & Hauff, F. (2011). Extent of the Ross Orogen in Antarctica: new data from DSDP 270 and Iselin Bank. *Antarctic Science*, *23*(3), 297–306. https://doi.org/10.1017/S0954102010000969

Mouginot, J., Rignot, E., & Scheuchl, B. (2019). Continent-wide, interferometric SAR phase, mapping of Antarctic ice velocity. *Geophysical Research Letters*, *46*(16), 9710–9718. https://doi.org/10.1029/2019GL083826

Muto, A., Christianson, K., Horgan, H. J., Anandakrishnan, S., & Alley, R. B. (2013). Bathymetry and geological structures beneath the Ross Ice Shelf at the mouth of Whillans Ice Stream, West Antarctica, modeled from ground-based gravity measurements. *Journal of Geophysical Research: Solid Earth*, *118*(8), 4535–4546. https://doi.org/10.1002/jgrb.50315

Müller, R. D., Gohl, K., Cande, S. C., Goncharov, A., & Golynsky, A. V. (2007). Eocene to Miocene geometry of the West Antarctic Rift System. *Australian Journal of Earth Sciences*, *54*(8), 1033–1045. https://doi.org/10.1080/08120090701615691

Paulsen, T., Encarnación, J., & Grunow, A. (2004). Structure and timing of transpressional deformation in the Shackleton Glacier area, Ross orogen, Antarctica. *Journal of the Geological Society*, *161*(6), 1027–1038. https://doi.org/10.1144/0016-764903-040

Paxman, G. J. G., Jamieson, S. S., Hochmuth, K., Gohl, K., Bentley, M. J., Leitchenkov, G., & Ferraccioli, F. (2019). Reconstructions of Antarctic topography since the Eocene–Oligocene boundary. *Palaeogeography, Palaeoclimatology, Palaeoecology*, *535*, 109346. https://doi.org/10.1016/j.palaeo.2019.109346

Pekar, S. F., DeConto, R. M., & Harwood, D. M. (2006). Resolving a late Oligocene conundrum: Deep-sea warming and Antarctic glaciation. *Palaeogeography, Palaeoclimatology, Palaeoecology*, *231*, 29–40. https://doi.org/10.1016/j.palaeo.2005.07.024

Piotrowski, J. A. (2006). Groundwater under ice sheets and glaciers. In P. G. Knight (Ed.), *Glacier Science and Environmental Change* (pp. 50–60). Malden, MA, USA: Blackwell Publishing. https://doi.org/10.1002/9780470750636.ch9

Pérez, L. F., De Santis, L., McKay, R. M., Larter, R. D., Ash, J., Bart, P. J., ... 374 Scientists, I. O. D. P. E. (2021). Early and middle Miocene ice sheet dynamics in the Ross Sea: Results from integrated core-log-seismic interpretation. *GSA Bulletin*. https://doi.org/10.1130/B35814.1

Rignot, E., Mouginot, J., Morlighem, M., Seroussi, H., & Scheuchl, B. (2014). Widespread, rapid grounding line retreat of Pine Island, Thwaites, Smith, and Kohler glaciers, West Antarctica, from 1992 to 2011. *Geophysical Research Letters*, *41*(10), 3502–3509. https://doi.org/10.1002/2014GL060140

Rignot, E., Mouginot, J., & Scheuchl, B. (2011). Antarctic grounding line mapping from differential satellite radar interferometry. *Geophysical Research Letters*, *38*, 1–6. https://doi.org/10.1029/2011GL047109

Rignot, E., & Scheuchl, B. (2016). MEaSUREs Antarctic grounding line from differential satellite radar interferometry, version 2. *Boulder, Colorado USA. NASA National Snow and Ice Data Center Distributed Active Archive Center*. https://doi.org/10.5067/IKBWW4RYHF1Q

Robertson, J. D., & Bentley, C. R. (1989). The Ross Ice Shelf: Glaciology and geophysics paper 3: Seismic studies on the grid western half of the Ross Ice Shelf: RIGGS I and RIGGS II. In C. R. Bentley & D. E. Hayes (Eds.), *Antarctic Research Series* (Vol. 42, pp. 55–86). Washington, D. C.: American Geophysical Union. https://doi.org/10.1029/AR042p0055

Rooney, S. T., Blankenship, D. D., & Bentley, C. R. (1987). Seismic refraction measurements of crustal structure in West Antarctica. In G. D. Mckenzie (Ed.), *Geophysical Monograph Series* (pp. 1–7). Washington, D. C.: American Geophysical Union. https://doi.org/10.1029/GM040p0001

Salvini, F., Brancolini, G., Busetti, M., Storti, F., Mazzarini, F., & Coren, F. (1997). Cenozoic geodynamics of the Ross Sea region, Antarctica: Crustal extension, intraplate strike-slip faulting, and tectonic inheritance. *Journal of Geophysical Research: Solid Earth*, *102*(B11), 24669–24696. https://doi.org/10.1029/97JB01643

Sauli, C., Sorlien, C., Busetti, M., De Santis, L., Geletti, R., Wardell, N., & Luyendyk, B. P. (2021). Neogene development of the Terror Rift, western Ross Sea, Antarctica. *Geochemistry, Geophysics, Geosystems*, *22*(3). https://doi.org/10.1029/2020GC009076

Scambos, T., Haran, T., Fahnestock, M., Painter, T., & Bohlander, J. (2007). MODIS-based Mosaic of Antarctica (MOA) data sets: Continent-wide surface morphology and snow grain size. *Remote Sensing of Environment*, *111*(2-3), 242–257. https://doi.org/10.1016/j.rse.2006.12.020

Shen, W., Wiens, D. A., Anandakrishnan, S., Aster, R. C., Gerstoft, P., Bromirski, P. D., … Winberry, J. P. (2018). The crust and upper mantle structure of Central and West Antarctica from bayesian inversion of Rayleigh wave and receiver functions. *Journal of Geophysical Research: Solid Earth*, *123*(9), 7824–7849. https://doi.org/10.1029/2017JB015346

Shen, W., Wiens, D. A., Lloyd, A. J., & Nyblade, A. A. (2020). A geothermal heat flux map of Antarctica empirically constrained by seismic structure. *Geophysical Research Letters*, *47*(14). https://doi.org/10.1029/2020GL086955

Siddoway, C. S. (2008). Tectonics of the West Antarctic Rift System: New light on the history and dynamics of distributed intracontinental extension. In A. K. Cooper et al. (Eds.), *Antarctica: A Keystone in a Changing World.* Washington DC: The National Academies Press.

Siegert, M. J., Kulessa, B., Bougamont, M., Christoffersen, P., Key, K., Andersen, K. R., … Smith, A. M. (2018). Antarctic subglacial groundwater: a concept paper on its measurement and potential influence on ice flow. *Geological Society, London, Special Publications*, *461*(1), 197–213. https://doi.org/10.1144/SP461.8

Smith, W. H. F., & Wessel, P. (1990). Gridding with continuous curvature splines in tension. *GEOPHYSICS*, *55*(3), 293–305. https://doi.org/10.1190/1.1442837

Sorlien, C. C., Luyendyk, B., Wilson, D. S., Decesari, R. C., Bartek, L. R., & Diebold, J. B. (2007). Oligocene development of the West Antarctic Ice Sheet recorded in eastern Ross Sea strata. *Geology*, *35*(5), 467. https://doi.org/10.1130/G23387A.1

Stern, T. A., Davey, F. J., & Delisle, G. (1991). Lithospheric flexure induced by the load of the Ross Archipelago, southern Victoria land, Antarctica. In M. Thomson, A. Crame, & J. Thomson (Eds.), *Geological Evolution of Antarctica* (pp. 323–328). Cambridge, UK: Cambridge University Press.

Still, H., Campbell, A., & Hulbe, C. (2019). Mechanical analysis of pinning points in the Ross Ice Shelf, Antarctica. *Annals of Glaciology*, *60*(78), 32–41. https://doi.org/10.1017/aog.2018.31

Studinger, M., Bell, R., Fitzgerald, P., & Buck, W. (2006). Crustal architecture of the Transantarctic Mountains between the Scott and Reedy Glacier region and South Pole from aerogeophysical data. *Earth and Planetary Science Letters*, *250*(1-2), 182–199. https://doi.org/10.1016/j.epsl.2006.07.035

ten Brink, U. S., Bannister, S., Beaudoin, B. C., & Stern, T. A. (1993). Geophysical investigations of the tectonic boundary between East and West Antarctica. *Science*, *261*(5117), 45–50. https://doi.org/10.1126/science.261.5117.45

Tinto, K. J., Padman, L., Siddoway, C. S., Springer, S. R., Fricker, H. A., Das, I., … Bell, R. E. (2019). Ross Ice Shelf response to climate driven by the tectonic imprint on seafloor bathymetry. *Nature Geoscience*, *12*(6), 441–449. https://doi.org/10.1038/s41561-019-0370-2

Tulaczyk, S., Kamb, B., Scherer, R. P., & Engelhardt, H. F. (1998). Sedimentary processes at the base of a West Antarctic ice stream: Constraints from textural and compositional properties of subglacial debris. *Journal of Sedimentary Research*, *68*(3), 487–496. https://doi.org/10.2110/jsr.68.487

Uieda, L., Tian, D., Leong, W. J., Jones, M., Schlitzer, W., Toney, L., … Wessel, P. (2021). *PyGMT: A Python interface for the Generic Mapping Tools.* Zenodo. https://doi.org/10.5281/zenodo.5607255

Venturelli, R. A., Siegfried, M. R., Roush, K. A., Li, W., Burnett, J., Zook, R., … Rosenheim, B. E. (2020). Mid-Holocene grounding line retreat and readvance at Whillans Ice Stream, West Antarctica. *Geophysical Research Letters*, *47*(15). https://doi.org/10.1029/2020GL088476

Werner, S. (1953). Interpretation of magnetic anomalies at sheet-like bodies. In *Sveriges Geologiska Undersok* (pp. 413–449). Stockholm Norstedt.

Wessel, P., Luis, J. F., Uieda, L., Scharroo, R., Wobbe, F., Smith, W. H. F., & Tian, D. (2019). The Generic Mapping Tools version 6. *Geochemistry, Geophysics, Geosystems*, *20*(11), 5556–5564. https://doi.org/10.1029/2019GC008515

Whitehouse, P. L., Gomez, N., King, M. A., & Wiens, D. A. (2019). Solid Earth change and the evolution of the Antarctic Ice Sheet. *Nature Communications*, *10*(1), 503. https://doi.org/10.1038/s41467-018-08068-y

Wilson, D. S., Jamieson, S. S., Barrett, P. J., Leitchenkov, G., Gohl, K., & Larter, R. D. (2012). Antarctic topography at the Eocene–Oligocene boundary. *Palaeogeography, Palaeoclimatology, Palaeoecology*, *335-336*, 24–34. https://doi.org/10.1016/j.palaeo.2011.05.028

Wilson, D. S., & Luyendyk, B. (2009). West Antarctic paleotopography estimated at the Eocene-Oligocene climate transition. *Geophysical Research Letters*, *36*(16), L16302. https://doi.org/10.1029/2009GL039297

Wilson, D. S., Pollard, D., DeConto, R. M., Jamieson, S. S., & Luyendyk, B. (2013). Initiation of the West Antarctic Ice Sheet and estimates of total Antarctic ice volume in the earliest Oligocene. *Geophysical Research Letters*, *40*(16), 4305–4309. https://doi.org/10.1002/grl.50797

*Geophysical Research Letters*

Supporting Information for

# Basement topography and sediment thickness beneath Antarctica's Ross Ice Shelf

M.D. Tankersley[1,2], H.J. Horgan[1], C.S. Siddoway[3], F. Caratori Tontini[2,4], K.J. Tinto[5]

[1]Antarctic Research Centre, Victoria University of Wellington, Wellington, New Zealand
[2]GNS Science, Lower Hutt, New Zealand
[3]Colorado College, Colorado Springs, CO, USA
[4]University of Genoa, Genoa, Italy
[5]Lamont-Doherty Earth Observatory, Columbia University, Palisades, NY, USA

## Contents of this file



## Introduction

This supplement provides additional information on the collection and processing of aeromagnetic line data (**Text S1**), the methodology of tying ROSETTA-Ice magnetic basement to ANTOSTRAT acoustic basement (Brancolini et al., 1995), through the use of Operation IceBridge( OIB) magnetic data (Cochran et al. 2014) (**Text S2 and S3**), the gridding, merging, and filtering of the resulting basement grid (**Text S4**), the calculation of sediment thickness and $\beta$-factors for the region (**Text S5**), and our quantification of uncertainties and comparison with points of previously measured sediment thickness (**Text S6**). Sediment thickness comparisons with past seismic surveys are included in **Table S1**. Also included are supplementary figures showing various additional Ross Ice Shelf grids (**Figure S1**), the Werner deconvolution solutions of OIB flight 403.3 (**Figure S2**), several selected ROSETTA-Ice flight lines with Werner deconvolution solutions (**Figure S3**), unfiltered basement solutions with flight line locations and individual Werner deconvolution solutions (**Figure S4**), and uncertainties applied to basement and sediment thickness results (**Figure S5**). Python code, within a Jupyter notebook, documents our workflow and figure creation, and is accessible here: https://zenodo.org/badge/latestdoi/470814953

**Text S1. Magnetic data collection, processing, and Werner deconvolution**

Both ROSETTA-Ice and OIB data sets were collected with a Scintrex CS3 Cesium magnetometer. Average flight speeds were 123 m/s and 93 m/s for OIB and ROSETTA-Ice respectively. Altitudes for the sections of OIB flight 403 used here average around 400 m above sea level, while ROSETTA-Ice altitude averaged at 750 m above ground level. OIB data were resampled from 20Hz to 1Hz to match the frequency of the ROSETTA-Ice data. Both datasets have been despiked, diurnally corrected, and had the International Geomagnetic Reference Field model removed. See Tinto et al. (2019) for more details of the ROSETTA-Ice survey and flight line locations. Due to variable flight elevations, both between and within the datasets, all magnetic data were upward-continued to 1000 m above sea level. To avoid artefacts of downwards continuing, any data with flight elevations above 1000 m were removed.

Here we use 2D Werner deconvolution (Werner, 1953, Ku & Sharp, 1983), applied to aeromagnetic line data, to image the shallowest magnetic signals in the crust. Assuming that the overlying sediments produce smaller magnetic anomalies than the crystalline basement, we treat the resulting solutions as a depth to the magnetic basement. During Werner deconvolution, moving and expanding windows are passed over the magnetic anomaly line data. Within each window, after linearly detrending the data, the source parameters of the anomalies are estimated with a least-squares approach, assuming the source bodies are infinite-depth dikes or contacts. The source parameters include position (distance along profile and depth), magnetic susceptibility, and source geometry (contact or dike). Solutions are considered valid between 1200 m and 20 km of upward continued flight elevation (approx. 200 m - 19 km bsl). Windows ranged from 500 m - 50 km, with a window shift increment of 1 km and an expansion of 1 km.

Due to passing over the data many times with varying window widths, Werner deconvolution produces a depth-scatter of solutions, which tend to cluster vertically beneath the true magnetic sources. Each of these solutions consists of location, depth, susceptibility (S), window width (W), and a simplified source geometry (dike or contact). For contact-type solutions, parameter S is the estimated magnetic susceptibility of the body, while for dike-type solutions, S is the product of susceptibility and dike width. During filtering (Text S2-3), a cut-off based on parameter S is used to remove shallow solutions. Since the value of parameter S for contact solutions are typically much smaller than for dike solutions (since they are not multiplied by dike width), only dike solutions have been considered here. To achieve a basement surface from this resulting depth-scatter of solutions, we have utilized parameter-based filtering and clustering, described in Text S2-3. This Werner deconvolution process was the same for both OIB and ROSETTA-Ice magnetics data. Werner deconvolution was performed in Geosoft's Oasis Montaj and subsequent processing of these results was performed in Python, and is included in a Jupyter notebook; https://zenodo.org/badge/latestdoi/470814953.

This magnetic basement approach has been used to map sedimentary basins throughout Antarctica, including the Ross Sea (Karner et al., 2005), western Marie Byrd Land (Bell et al., 2006), and Wilkes Subglacial Basin (Studinger et al., 2004; Frederick et al., 2016. Our approach is similar to past studies, but our proximity to well-constrained offshore seismic basement depths (Brancolini et al., 1995) allows us to develop the method further. Most studies display their results as 2D profiles with the depth-scatter of solutions mentioned above, and simply use the tops of the clusters as the basement depth. By comparison with seismic basement, we have developed a reliable, automated method of 'draping' a surface over these depth-scattered solutions to produce a 3D surface. This process is described below.

**Text S2. Tying magnetic basement to seismic basement**

To validate this method and address uncertainty we perform Werner deconvolution for OIB magnetics data (Figure 1b, Cochran et al., 2014) over the Ross Sea. Here, ice-free conditions have permitted shipborne seismic surveys to image basement depths in the region. These have been compiled by the Antarctic Offshore Acoustic Stratigraphy project (ANTOSTRAT) (Brancolini et al., 1995) (Figure 1b). The basement was not imaged for the deeper portions of the basins and data coverage of actual basement reflectors, versus interpolation between basement reflectors, is not reported. Werner deconvolution (Text S1) produces a series of many solutions (black dots in Figures 2 & S2) at each window along the line.

To achieve a basement surface, instead of a depth-scatter of solutions, solutions were filtered based on Werner window width (W) and the product of magnetic susceptibility and body width (parameter S). Filtered solutions (black circles, scaled to parameter S in Figures 2 & S2) were then horizontally binned with variable bin sizes (parameter B) (vertical grey lines in Figures 2 & S2). Bins with a minimum count of solutions (parameter C) were retained, and the depth of the bin center was set to the $95^{th}$-percentile depth of the solutions in the bin. This removed spurious shallow solutions, while effectively retaining the 'top' of the magnetic signal. These bin centers (orange crosses in Figures 2 & S2) were then interpolated, producing our model of magnetic basement depths (orange line in Figures 2 & S2). The above filtering techniques removed the solutions above the basement, and the clustering technique fitted a surface over the remaining points, which represents the top of the basement. This interpolated line allowed a direct comparison between ANTOSTRAT seismic basement and OIB magnetic basement.

We varied each of the four parameters (W, S, B, and C) with 21 different values and conducted the above procedures for all unique combinations of them on OIB line 403, segments 1 and 3, in the Ross Sea (location in Figure 1b). This resulted in 194,481 iterations, for each of which we calculated a mean absolute difference at points every 5km between ANTOSTRAT seismic basement and the resulting OIB magnetic basement. We found the parameter values which produced the closest match between OIB magnetic basement and ANTOSTRAT seismic basement, as shown in Figures 2 & S2. These resulting values were a maximum Werner deconvolution window width (parameter W) of 10 km, a minimum product of magnetic susceptibility and body width (parameter S) of 1.0, a horizontal bin width (parameter B) of 36 km, and a minimum number of solutions per bin (parameter C) of 6. The median absolute misfit between OIB and ANTOSTRAT basement for the two line-segments was 480 m (270 m for Line 403-1 (Figure 2), and 1060 m for Line 403-3 (Figure S2)). This equates to 11% of ANTOSTRAT depths. The close fit between the OIB magnetic basement and the ANTOSTRAT seismic basement both supports the validity of this method and gives us the parameters necessary to repeat this method for data over the RIS.

**Text S3. Tying Ross Sea magnetic basement to Ross Ice Shelf magnetic basement**

Having optimized our method to match OIB magnetic basement to ANTOSTRAT seismic basement in the Ross Sea (Text S2, Figures 2 & S2), we now optimize the method to match ROSETTA-Ice magnetic basement to OIB magnetic basement. This additional optimization is necessary due to differences in processing and survey design, including flight elevations, speed, aircraft, mounting equipment used, and frequency of recording. With the optimized parameters for OIB data (Text S2), we calculate magnetic basement for OIB flight 404 over the ice shelf. We treat this as the 'true' basement and update the filtering and clustering parameters (Text S1) to minimize the misfit between OIB basement and the resulting ROSETTA-Ice basement. This tuning was performed on ROSETTA-Ice lines 590 and 650, which were coincident with segments from OIB line 404 (location in Figures 1b & S4). Optimal parameters to match ROSETTA-Ice solutions to OIB basement are found to be W<26 km, S>1.2, B=36 km, and C>40, resulting in a median absolute misfit between OIB basement and ROSETTA-Ice solutions of 400 m (22% of OIB depth). With these parameters which best match ROSETTA magnetic basement to OIB magnetic basement, we performed the same procedure on all the ROSETTA-ice flight lines. A selection of these lines, and the two ties to OIB 404, are shown in Figure S3.

**Text S4. Gridding, merging, and filtering**

The above processes were performed on all ROSETTA-ice flight lines (white lines in Figure S4), including the N-S tie lines at ~55 km spacing. Where the tie lines crossed over the E-W flights lines, some resulting basement solutions (black dots in Figure S4) are nearby those from the crossing line. Since we are interested in the shallowest magnetic signals, we have retained only the shallowest solution with 8km cells across our region. Since bin widths (parameter B) were set to 36 km, the nearest solutions along individual lines were further apart than the 8km cell. The closest spacing of E-W flight lines was 10 km, so this process only affected solutions at the crossover between N-S and E-W lines. These points were then gridded with a 5 km cell size and a minimum curvature spline with a tension factor of 0.35 (Smith & Wessel, 1990) (Figure S4). This grid was then merged with a Ross Sea seismic basement grid. The Ross Sea grid, while mostly ANTOSTRAT data, was sourced from a regional compilation of sediment thicknesses (Lindeque et al., 2016, Wilson and Luyendyk 2009), we have subtracted from bathymetry depths (Morlighem et al. 2020) to achieve basement depths. Where the grids overlap near the ice shelf edge, we retain our RIS values. To aid in the merging at the overlaps, and to match RIS basement wavelengths to the characteristic basement wavelengths of ANTOSTRAT, we filtered the merged grid with an 80 km Gaussian filter (Figure 3a). This filtering was performed with a variety of wavelengths (20-120 km), where we found filters < 80 km didn't significantly alter the regional basement, while filters > 80 km excessively smoothed the basement topography.

**Text S5. Sediment thickness and β-factor calculations**

With the regional basement model (Figure 3a) including RIS magnetic basement and offshore seismic basement, we calculated sediment thickness (Figure 3b) by subtracting the grid from Bedmachine bathymetry depths (Figure1a & S1e, Morlighem et al. 2020). Previous estimates of sediment thickness for the sub-RIS come from the extrapolation of gravity anomalies with bathymetry trends (Wilson and Luyendyk, 2009). These were included in the Lindeque et al. (2016) compilation (Figure S1d). Eocene-Oligocene boundary paleotopographic reconstructions (Wilson et al., 2012, Paxman et al., 2019) assumed this sediment estimate was post-Eocene and used it as their maximum sub-RIS sediment thickness, incorporated into their minimum surface reconstruction. The thickness of sediment affects onshore erosion estimates, surface raising due to deposition, and isostatic surface subsidence to due loading. For their maximum paleotopographic reconstructions, they used a thinner sediment model, with the same general trends (Wilson & Luyendyk, 2009). Figure S1 (c, d, & f) shows the comparison between the sediment thickness models. Figure S1f colorbar histogram shows the distribution, with our values having a mean thickness ~115m greater than the past model. Yet, along the Siple Coast, we show much greater discrepancies, up to 2 km thicker.

$\beta$-factor, the ratio of initial crustal thickness to final crustal thickness, is useful for quantifying the thinning of crust in extensional settings. We calculate a distribution of $\beta$-factors beneath the RIS by assuming a uniform initial crustal thickness and dividing it by current crustal thickness. We pick an initial crustal thickness of 38 km, which represents a global average for un-thinned plateau-type crust (Mooney et al., 1998), and has been used for the West Antarctic Rift System $\beta$-factor calculations (Müller et al., 2007). For the final (current) crustal thickness, we use a continent-wide Moho model from surface wave observations to define the bottom of the crust (An et al., 2015). For the top of the crust, we use our resulting RIS basement grid.

**Text S6. Uncertainty and assumptions**

We estimated a representative uncertainty for our basement model by examining the misfit of our modeled basement compared to offshore seismic basement depths (Brancolini et al., 1995). We did this by sampling our OIB magnetic basement estimate and the coincident ANTOSTRAT basement at 1 km intervals along lines 403-1 and 403-3 (Figures 2 and S2) and compared the values. The resulting absolute values of the differences don't exhibit a normal distribution; therefore, we use the median of the absolute misfit (+/-480m) as the basement model uncertainty. This equates to 22% of average basement depths for the sub-RIS. We performed a similar analysis between OIB magnetic basement and ROSETTA-Ice magnetic basement for coincident lines 590 and 650 (Figure S3 e & f). This resulted in a median absolute misfit of 400m. Tinto et al. (2019) report an uncertainty of 68m for their bathymetry model. Incorporating this with our basement model gives an uncertainty of 550m (37% of average thickness) for our sediment thickness results. Comparison with sub-RIS sediment thickness and distribution results from a variety of methods, including active source seismic surveys (Table S1 and references within), seismic radial anisotropy (Zhou et al., 2022), geophysical machine learning (Li et al. 2021), and magnetotelluric surveying (Gustafson et al. 2022, in review), all show general agreement with our results.

Our resulting basement grid is the depth to the shallowest magnetic signal. It is assumed that the crystalline basement in this region produces significantly larger magnetic anomalies compared to the overlying sediment fill. Note that in some instances, such as igneous bodies intruded into sedimentary basin fill, Werner-determined solutions fall upon the crest of the intrusion, and the actual top of the crystalline basement could be at a deeper level. Intrusions of small lateral extent will have small widths, resulting in small values of parameter S (susceptibility x width) and therefore will be removed by our filter (Text S2). For larger intrusions into existing basins, (i.e. Ross Island and Minna Bluff (Cox et al., 2019)), the modeled magnetic basement surface will be shallower than the bottom of the sedimentary basin. While this underestimates sediment volume, it better characterizes the competency of the substrate from an ice dynamics perspective. This is similar to how extensive intrusions into basins would be imaged by seismic surveys as shallow basement. However, these extensive regions of late-Cretaceous-Cenozoic magmatism are not expected to be prevalent under the RIS (Andrews et al., 2021).

| **Name** | **Reference** | **Seismic sediment thickness (m)** | **Magnetic sediment thickness (m)** | **Absolute difference (m)** |
|---|---|---|---|---|
| CIR | Rooney et al. (1987) | 400 | 504 | 104 |
| I10S | Robertson and Bentley (1989) | 750+/-100 | 1624 | 874 |
| J9DC | Greischar et al. (1992) | 1350 | 771 | 579 |
| BC | Robertson and Bentley (1989) | 1900+/-400 | 1124 | 776 |
| RI | Greischar et al. (1992) | 850 | 807 | 43 |
| C49 | Crary (1961) | 754 | 1162 | 408 |
| LAS | Crary (1961) | 1325 | 1820 | 495 |
| Q13 | Greischar et al. (1992) | 255+/-145 | 744 | 489 |

**Table S1.** Previous seismic sediment thickness results for the Ross Ice Shelf. Stations names are labeled in Figure 3b. Magnetic sediment thickness column shows our sampled results at the location of each station. Comparing the seismic estimates with our sediment thickness at the eight stations gives a median absolute misfit of 480m.

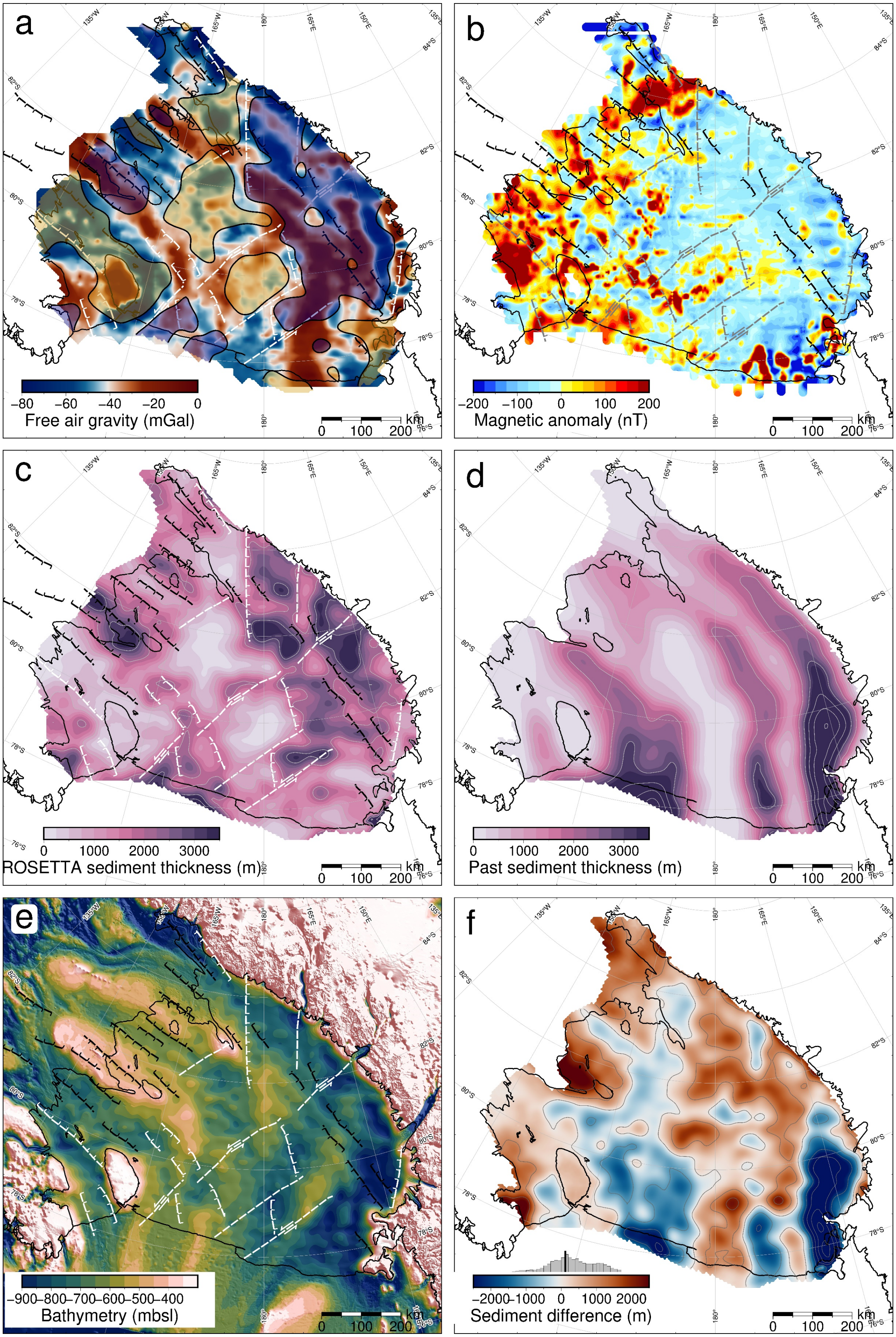
a
Free air gravity (mGal)
−80 −60 −40 −20 0
b
Magnetic anomaly (nT)
−200 −100 0 100 200
c
ROSETTA sediment thickness (m)
0 1000 2000 3000
d
Past sediment thickness (m)
0 1000 2000 3000
e
Bathymetry (mbsl)
−900 −800 −700 −600 −500 −400
f
Sediment difference (m)
−2000 −1000 0 1000 2000
km
0 100 200

**Figure S1. (a)** ROSETTA-Ice free air gravity (Tinto et al., 2019). Shaded yellow regions are shallow basement (<~1600 mbsl), shaded blue regions are deep basement (>~2600 mbsl). **(b)** ROSETTA-Ice airborne magnetic anomaly data (Tinto et al., 2019). **(c)** Sediment thickness from this study (same as Figure 3b), with 1 km contours. **(d)** Sediment thickness from a regional compilation (Text S5, Lindeque et al., 2016, Wilson & Luyendyk, 2009), with 1 km contours. **(e)** Bedmachine2 bathymetry (Morlighem et al., 2020), from which sediment thickness in (c) was calculated. **(f)** Difference between (c) and (d). Red signifies our results have more sediment, while blue signifies our results have less sediment. Histogram shows data distribution, with mean value (black) at 115m. Inferred faults in a),b),c), and e) same as Figure 4a. Grounding line and coastlines in black (Rignot et al., 2013). Projection is Antarctic Polar Stereographic: EPSG 3031.

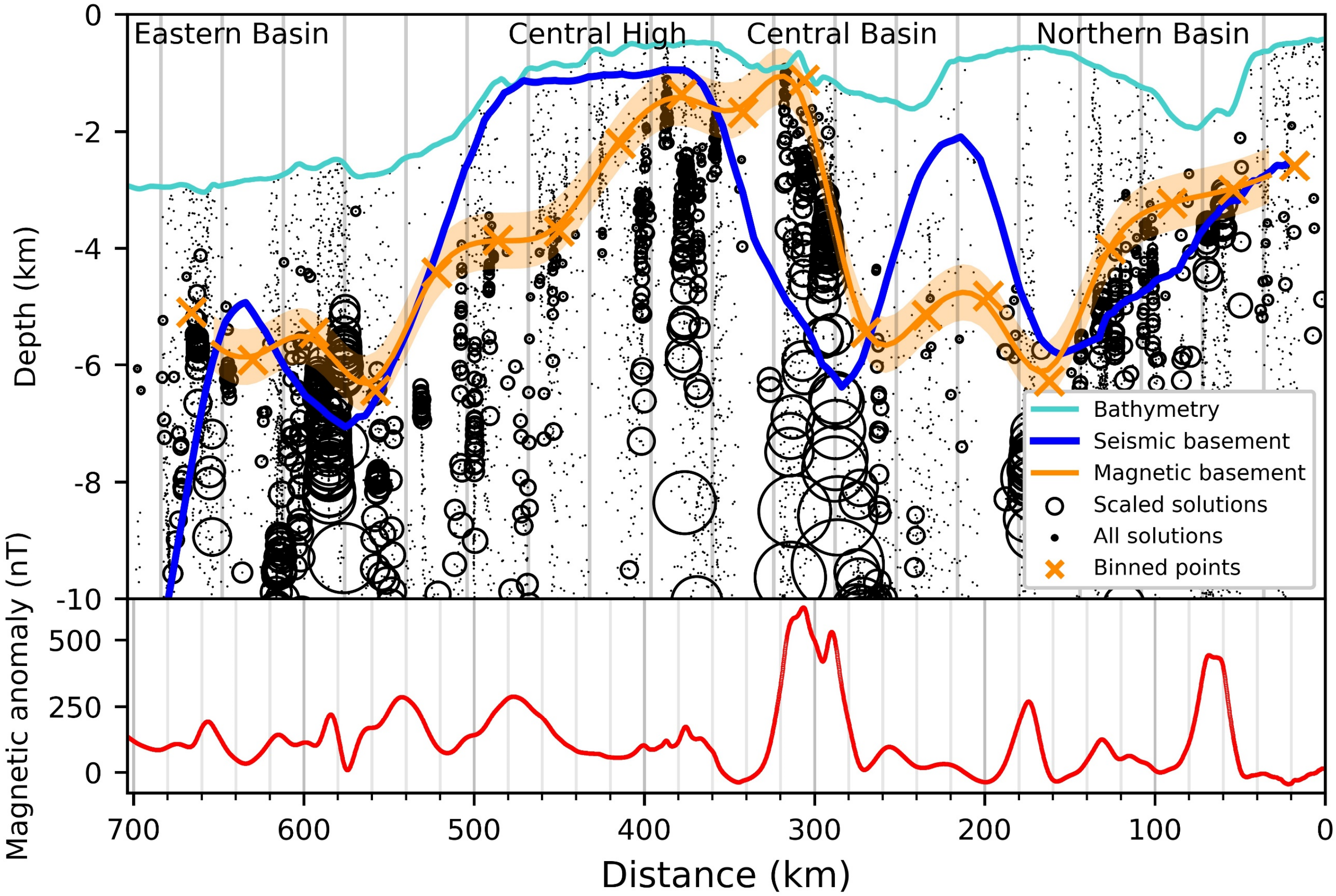


**Figure S2.** Ross Sea magnetic and seismic basement comparison. Operation IceBridge airborne magnetic data (lower panel) from segment 403-3 (Figure 1b). Small dots show Werner deconvolution solutions, which were filtered based on parameter S and W (Text S1) to produce black circles, which are scaled to parameter S. These circles were binned at a width equal to parameter B, shown by the vertical grey lines in the upper panel. Orange crosses show bin centers, which were fitted to a line to facilitate the comparison between the magnetic basement (orange line) and seismic basement (blue line). Orange band shows +/- 480m uncertainty for the basement model. Ross Sea basement features are labeled on top.

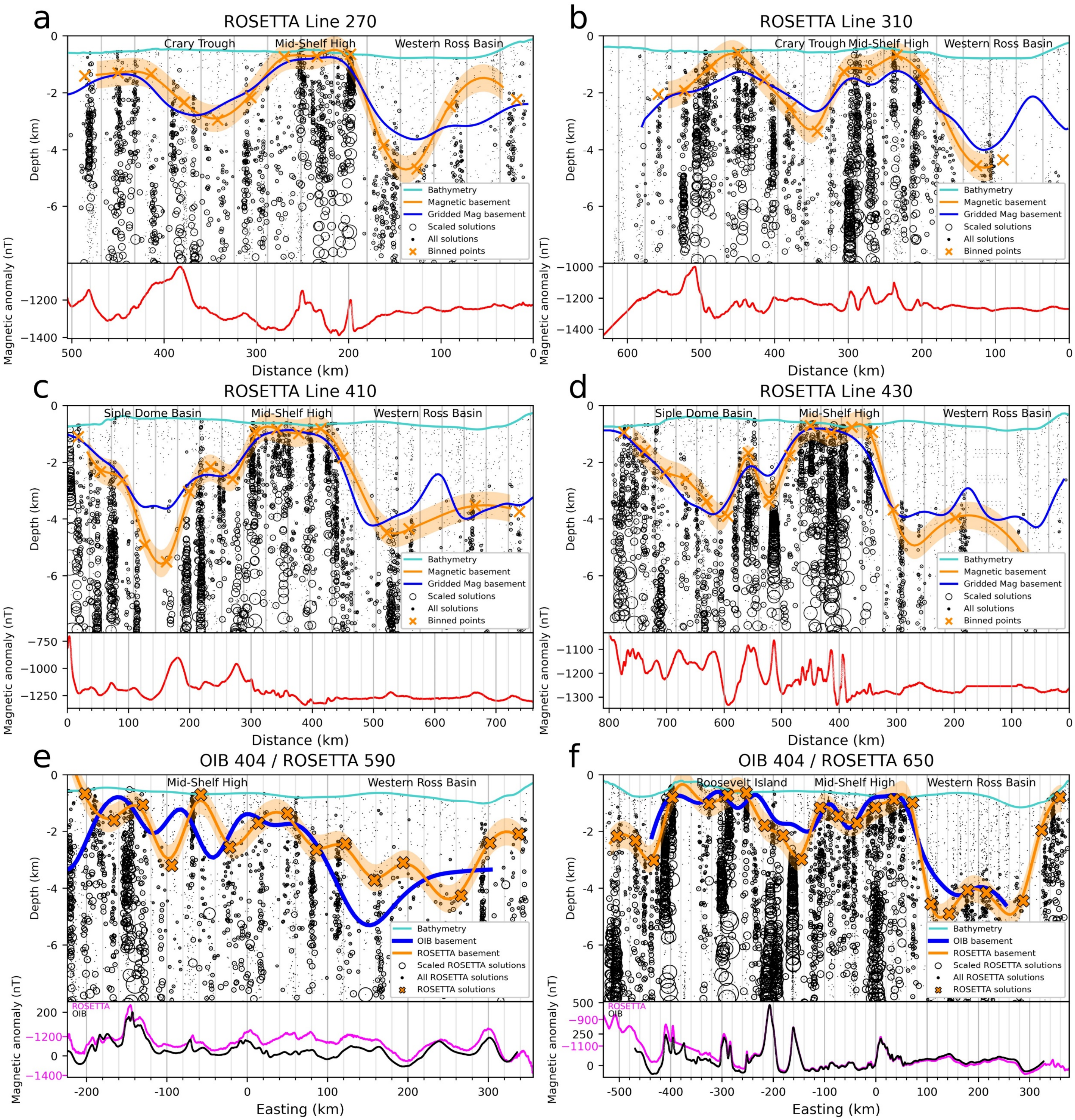


**Figure S3.** Werner deconvolution solutions for a selection of ROSETTA-Ice lines, locations highlighted in Figure S4. Bathymetry from Bedmap2 (Fretwell et al., 2013). Dots, circles, and vertical grey lines same as Figure S2. **a-d)** Comparison between magnetic basement before and after filtering and gridding. Orange crosses are magnetic basement solutions, shown as black dots inf Figure S4, and highlighted for these lines. Orange line with uncertainty bounds is fitted to these solutions. Blue lines are magnetic basement sampled from the grid of Figure 1a, after gridding and filtering. Red lines show ROSETTA-Ice magnetics data. **e-f)** Comparison between magnetic basement resulting from Werner deconvolution of coincident OIB and ROSETTA-Ice flight lines. Location is shown in Figures 1b and S4. These two lines were used to tie the ROSETTA-Ice survey to the OIB survey (Text S3). Blue lines are OIB magnetic basement results, orange crosses and fitted orange lines with uncertainty bands are ROSETTA-Ice magnetic basement. ROSETTA-Ice (pink) and OIB (black) magnetics data are shown in lower panels.

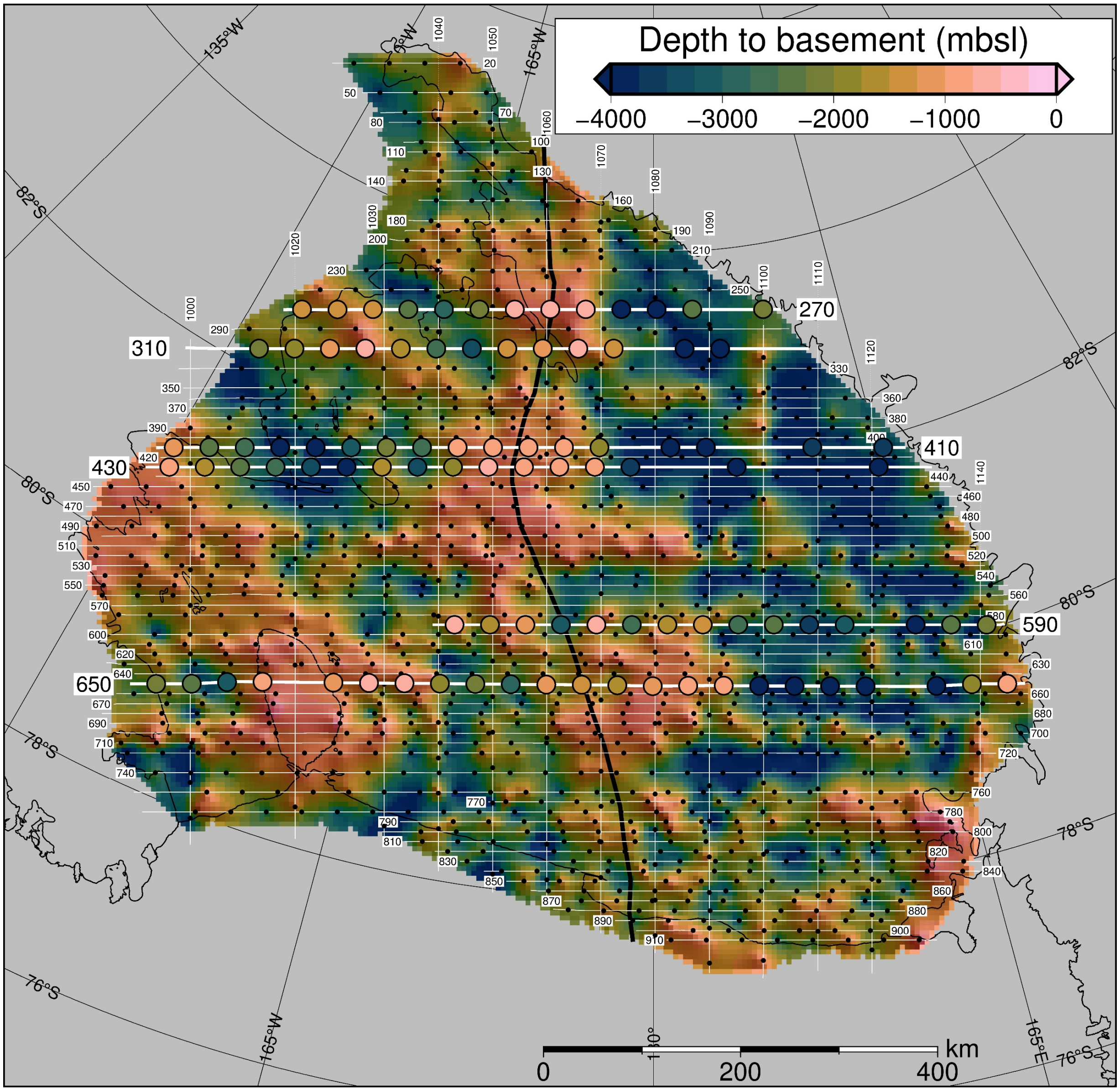


**Figure S4.** Unfiltered magnetic basement. Point solutions (black dots here, orange crosses in Figure S3) along ROSETTA-Ice flight lines (labeled) were gridded with a 5km cell size and a minimum curvature spline with a tension factor of 0.35. Figure S3 flight lines (bold white) and point solutions (colored circles) are shown. Black line through the Mid-Shelf High shows the East-West Antarctic divide used in colorbar histograms of Figures 3 and 4a. Grounding line and coastlines in black (Rignot et al., 2013).

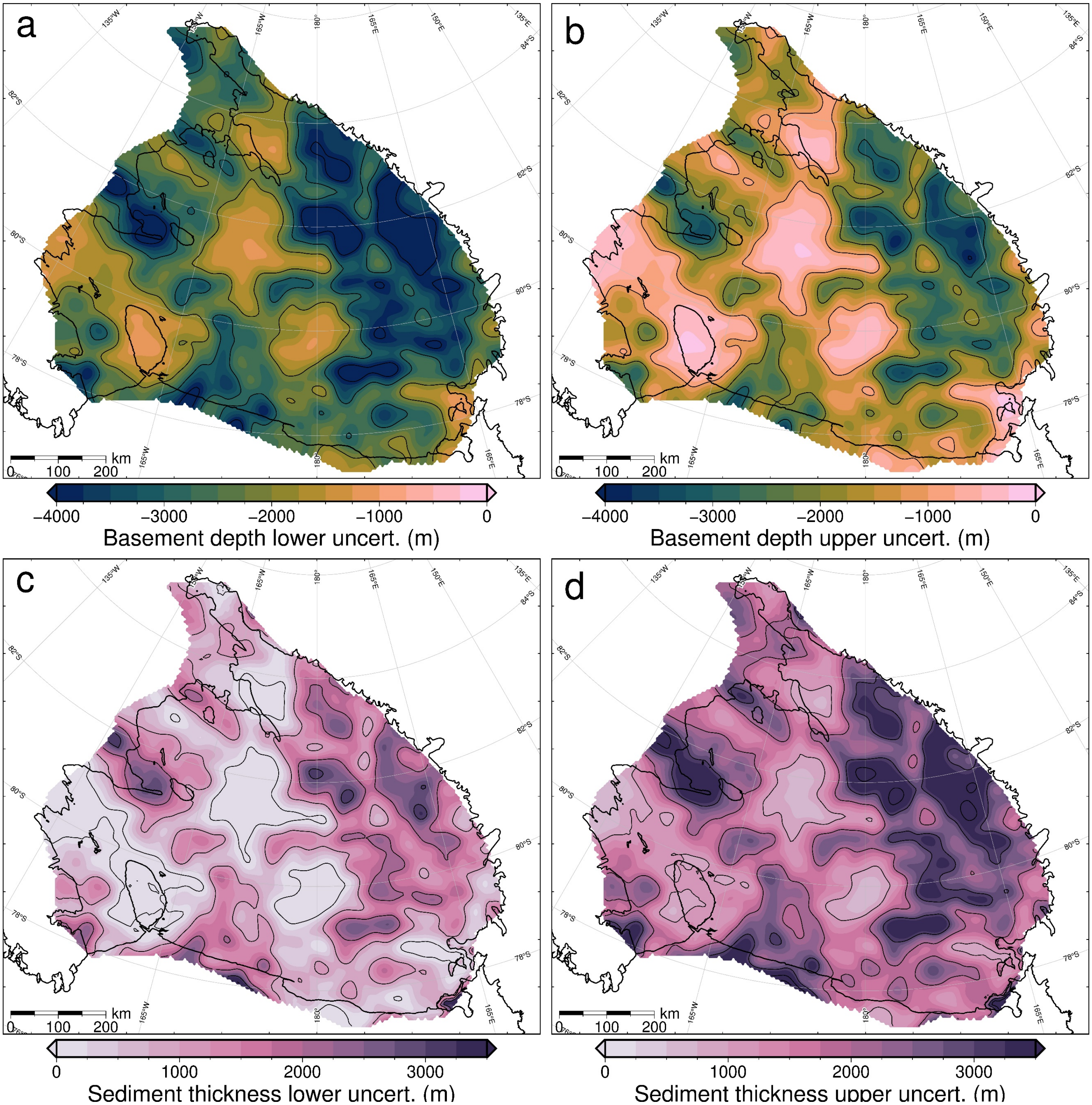


**Figure S5.** Upper and lower limits of uncertainty applied to **a-b)** magnetic basement and **c-d)** sediment thickness. See Text S6 for how these uncertainties were determined.